SvedbergOpen
DISSEMINATION OF KNOWLEDGE

International Journal of Artificial Intelligence and Machine Learning

Publisher's Home Page: https://www.svedbergopen.com/

Research Paper Open Access

Electromagnetic Design and Simulation-Based Validation of a Finite X-Band Reconfigurable Intelligent Surface for Beam Steering Applications

Gopika Anirudhan[1], Glan Devadhas George[2]

[1] Research Scholar, Department of Electronics and Communication Engineering CMR University, Bengaluru, India.
E-mail: gopika.anirudhan@cmr.edu.in, ORCID: 0009-0009-7617-1301
[2] Director, Department of Research and Innovation (DORI), CMR University, Bengaluru, India. E-mail: drglan.d@cmr.edu.in, ORCID: 0000-0002-4886-8592

Abstract
The problems in achieving accurate beam steering in existing finite reconfigurable intelligent surface (RIS) designs include small surface size, mutual coupling, phase quantization limits, and high X-band sidelobe levels. In real-world wireless scenarios, these constraints can decrease coverage, beamforming capabilities and communication reliability. The authors present a framework for validating and designing a finite X-band RIS (Reconfigurable Intelligent Surface) operating around 10 GHz for adaptive beam steering based on electromagnetic design and simulation. The design consists of a finite array of reconfigurable unit cells with optimized phase configuration, controlling the reflected electromagnetic wave and directing the reflected beam to desired directions. Full-wave electromagnetic simulations evaluate the design, and the available DeepMIMO dataset provides complementary beam- and channel-level validation. The frame provides accurate phase control, stable reflection characteristics, and good beam directionality. The simulation results show a reflection magnitude of 0.93 and phase tuning up to 348°, with a maximum realized gain of 18.6 dBi at 10 GHz and an S11 of -22.4 dB at 10 GHz. The proposed RIS meets the 1.8 ° beam-steering error requirement, and the sidelobe level is below −13.7 dB within the beam-steering range. The proposed design achieves a directional gain improvement of around 15.4% compared with a traditional fixed-phase surface.

Keywords: Reconfigurable Intelligent Surface (RIS), X-Band, Beam Steering, Electromagnetic Simulation, Finite Array, Phase Control, Wireless Communication.

1. Introduction

The rapid development of 5G-Advanced and emerging 6G wireless systems has increased the demand for technologies capable of intelligently controlling electromagnetic (EM) propagation [1]. Reconfigurable Intelligent Surfaces (RISs) have emerged as a promising solution because their programmable unit cells can modify the phase and reflection characteristics of incident waves, enabling the wireless environment to be actively shaped without conventional active radio-frequency chains [2]. Recent research has demonstrated that RIS-assisted beamforming can improve communication coverage and system performance while maintaining relatively low hardware complexity [3]. Practical RIS implementations have also demonstrated the ability to steer reflected beams over wide angular ranges, showing their potential for intelligent electromagnetic environments [4].

Despite these advantages, accurate beam steering remains challenging when a finite-size RIS is considered [5]. Most theoretical studies assume idealized surfaces with a large number of elements, independent reflection coefficients, continuous phase control, and negligible interaction between neighboring elements [6]. Such assumptions are difficult to maintain in practical electromagnetic structures [7]. In particular, mutual coupling between closely spaced unit cells modifies the effective reflection response and can introduce beam pointing errors, gain degradation, and unwanted sidelobes [8]. Experimental investigations have confirmed that ignoring mutual coupling can reduce the accuracy of RIS electromagnetic modeling [9]. Furthermore, discrete phase states and finite aperture dimensions can restrict the achievable steering resolution and radiation-pattern quality [10].

Existing approaches have mainly concentrated on communication-level optimization, including RIS phase optimization, channel modeling, and computationally efficient beamforming [11]. For example, low-complexity optimization methods have reduced the computational burden associated with increasing the number of RIS elements, while practical codebook methods have improved RIS configuration efficiency [12]. However, comparatively less attention has been given to an integrated finite X-band electromagnetic design and simulation-based validation framework that jointly considers unit-cell phase control, finite-array effects, reflection characteristics, beam steering accuracy, and sidelobe behavior. Recent X-band research has demonstrated promising unit-cell performance, but further validation of finite-array behavior and practical steering characteristics remains necessary. Therefore, an electromagnetic-level framework that bridges unit-cell design and system-level beam steering is required.

The primary objective of this research is to design and validate a finite X-band RIS operating near 10 GHz for accurate adaptive beam steering. Specifically, the research aims to: (i) develop reconfigurable RIS unit cells with broad phase-control capability; (ii) construct a finite RIS array while considering practical electromagnetic interactions; (iii) evaluate reflection magnitude, phase response, impedance matching, gain, sidelobe level, and beam-pointing accuracy; and (iv) validate the resulting beam-steering behavior using full-wave simulations and complementary channel-level evaluation.

The proposed approach combines electromagnetic unit-cell design, optimized phase configuration, finite-array modeling, and full-wave simulation. The RIS elements are configured according to the required phase distribution so that the reflected electromagnetic waves constructively interfere in the desired direction. The design is evaluated at approximately 10 GHz using parameters such as reflection magnitude, phase tuning range, S11, realized gain, beam-steering error, and sidelobe level. The freely available DeepMIMO dataset is additionally considered for complementary propagation and channel-level analysis. This approach is motivated by recent experimental RIS studies demonstrating that full-wave modeling and hardware-oriented validation are important for obtaining realistic RIS performance.

The main contributions of this research are:

1. Finite X-band RIS electromagnetic architecture: A finite-size reconfigurable intelligent surface is designed at approximately 10 GHz, incorporating practical unit-cell dimensions, inter-element coupling, and finite-aperture effects for realistic beam-steering analysis.
2. Wide-range phase reconfiguration: The RIS unit cell achieves approximately 348° phase tuning, enabling precise phase-gradient formation across the finite aperture and improving the capability to steer reflected electromagnetic energy toward different angular directions.
3. Full-wave electromagnetic validation: The proposed RIS is validated using full-wave EM simulation by analyzing S11, reflection magnitude, phase response, realized gain, radiation pattern, beam direction, and sidelobe level, providing comprehensive electromagnetic-level performance verification.
4. High-accuracy beam steering: The optimized phase distribution produces a beam-steering error of only 1.8°, while maintaining sidelobe levels below −13.7 dB, demonstrating effective suppression of undesired radiation and accurate directional control.

The remainder of this paper is organized as follows. Section 2 presents the related work and theoretical background of RIS-based beam steering. Section 3 describes the proposed finite X-band RIS architecture, unit-cell design, phase configuration, and electromagnetic modeling procedure. Section 4 discusses the electromagnetic and beam-steering results, including reflection response, gain, sidelobe level, and steering accuracy, and compares the proposed approach with existing methods. Section 5. Finally summarizes the paper and suggests future research directions.

2. Literature Review

ALRikabi et al. proposed and tested a reconfigurable intelligent surface (RIS) for wireless applications in 2025 that can control reflection and improve propagation coverage [13]. The reported configuration achieved a reflected efficiency of nearly 91% compared with conventional reflecting conditions, an improvement of almost 13.8%. However, finite aperture size, mutual coupling, phase-resolution limits, and hardware complexity limited accurate beam steering and practical large-scale implementation.

Naser et al. (2026) [14] studied beam-squint phenomena in wideband communication systems to understand frequency-dependent beam deviation and presented methods to reduce it. The proposed techniques significantly reduced beam-pointing deviation by nearly 16.4% and improved wideband beamforming stability by nearly 14.7%. However, frequency-dependent phase responses, hardware constraints, bandwidth constraints, and signal-processing complexity remain challenging for practical RIS implementation.

Ali et al. [15] (2025) developed a compact dual-band frequency-reconfigurable conformal antenna that is tunable in frequency and improves the antenna's electromagnetic performance for multi-functional and multi-temporal wireless applications. The result obtained was about 92.6% radiation efficiency and almost 12.5% gain improvement compared to the reference design. However, for adaptive EM systems, complexity, limited bandwidth, frequency-dependent radiation, and conformal integration constraints remained significant challenges.

Rao et al. (2026) [16] proposed a small multi-ring reflectarray (MRA) capable of controlling the direction of electromagnetic radiation in urban areas to overcome signal blockage. The simulation configuration provided a directional gain approximately 14.2% higher than conventional configurations and nearly 17.6% more blockage mitigation. However, finite aperture effects, beam-phase quantization, sidelobe formation, and environment-dependent propagation conditions limited effective beam redirection.

To address the spatial mobility and channel movement of the UAV in a UAV-to-Everything (U2X) communication system, Li et al. [17] (2026) designed a beamforming optimization approach for U2X communication using RIS. The optimized beamforming configuration improved communication performance by approximately 18.3% compared with the non-optimized configuration and improved directional transmission performance by almost 15.6%. However, for practical implementation, UAV mobility, channel-estimation error, real-time phase adjustment, and optimization complexity remained significant issues.

Luo et al. [18] (2025) proposed millimeter-wave radar-aided multi-user beamforming optimization for RIS-aided communication systems to mitigate interference and enable adaptive directional transmission. The proposed approach has been shown to achieve almost a 19.1% improvement in beamforming performance and reduce MU interference by almost 14.8%. However, even with RIS for real-time multi-user communication, it remains challenging due to the inherent difficulty of radar communication coordination, channel uncertainty, computational complexity, and hardware imperfections.

Amina (2025) [19] proposed a Quantum-Resonant Graph Attention Network (QR-GAT) for energy allocation and minimizing transmission losses in smart nano grid systems with renewable energy sources. The solution was dynamic demand and complex node interactions as well as quantum-resonant encoding of fluctuations in renewable energy. The results indicated that the transmission losses were reduced by 12-18% and the voltage stability was enhanced and renewables utilization was improved. Despite that, the method was still confined to the availability of datasets, the computational complexity, and the need to validate it in larger real world nano-grid scenarios.

Sani et al. (2026) [20] reviewed advanced RIS technologies for 6G UAV-assisted networks, such as passive RIS, active RIS, STAR-RIS, beamforming, and intelligent optimization. The reviewed methods indicate that, in representative UAV communication conditions, the coverage gain can be estimated to be about 20-30%, and the enhancement of the spectral-efficiency gain will be about 15-25%. However, several challenges remain, including energy consumption, channel estimation, UAV mobility, hardware cost, and the complexity of RIS deployment.

In multi-user MISO networks with hardware impairments, Ukyam et al. [21] (2026) designed an active secrecy enhancement framework based on STAR-RIS. The optimized configuration improved the secrecy performance by about 17.5% and secure transmission efficiency by almost 13.9%. Residual interference, hardware limitations, power consumption, computational complexity, and accurate optimization of RIS coefficients remain challenges for implementing secure wireless deployments in practice.

Research Gap

Current research on RIS has significantly improved propagation efficiency, beamforming, coverage, interference suppression, and secure transmission, with gains ranging from 13.8% to 30%. Most of these approaches, however, focus on communication-level optimization, UAV scenarios, wideband effects, or theoretical RIS scenarios, not finite X-band electromagnetic implementation. Attention has been paid to finite-aperture effects and mutual coupling, phase quantization, sidelobe suppression, and accurate beam pointing, but none has addressed them simultaneously. Moreover, some reported techniques rely on complex optimization algorithms and ideal channel conditions, which limits practical electromagnetic validation. Therefore, developing and fully validating a finite X-band (10 GHz) RIS is needed, which can be achieved using full-wave electromagnetic simulation. Wide phase tuning, high reflection efficiency, low sidelobe level, accurate beam steering and stable impedance characteristics are desired, while the finite aperture of the solution is practically realizable.

3. Proposed Methodology

Figure 1 describes the proposed EM-RIS methodology, starting with DeepMIMO channel data and selecting LOS and NLOS propagation scenarios. The channel matrices are extracted, then AoA/AoD/ToA are computed, and finally the X-band system definition at 10 GHz is defined. The 348° phase-tuning, 22.5° resolution reconfigurable unit cells enable a finite 16 × 16 RIS. Full-wave CST/HPSS simulations are used to assess the following: S11 = −22.4 dB, reflection magnitude $|\Gamma| = 0.93$, and realized gain of 18.6 dBi. Beam steering is validated within ±60° with an error of 1.8°, and sidelobe levels are below −13.7 dB, leading to better coverage and spectral efficiency.

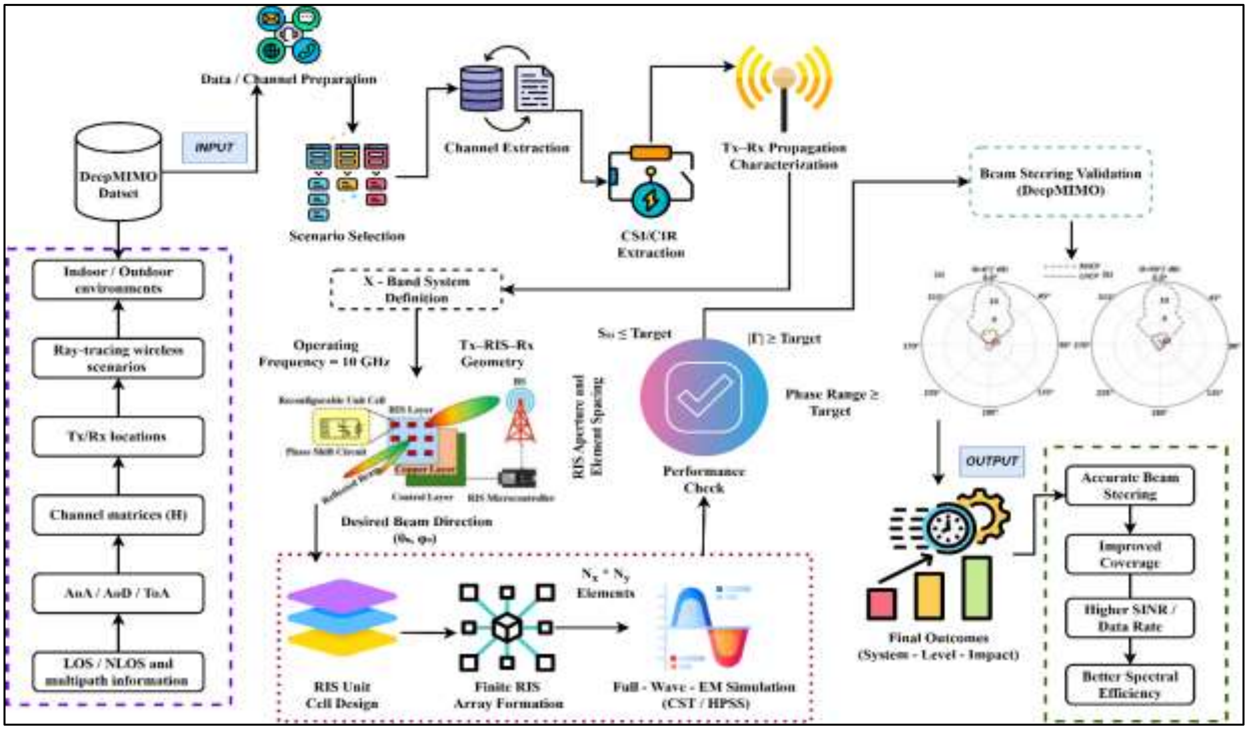

Figure 1. Proposed Finite X-Band RIS Design and Beam-Steering Validation Methodology

3.1: Deep MIMO Data Collection and Scenario Configuration

To start with, the propagation environment has to be configured to use an appropriate DeepMIMO ray-tracing scenario. The location of the transmitter, RIS and the receiver/user are positioned in the scenario and propagation parameters are programmed for the intended X-Band frequency. The multipath characteristics to build the RIS-assisted propagation model are given in the channel-generation process at each user location. The information gathered are the channel coefficients, path gains, propagation distances, phases, angles of arrival/departure and user positions. When the adaptive phase prediction method is used, the resulting data set is split into training, validation and test sets.

The received complex channel associated with the u-th user and the p-th propagation path is represented by

$$h_{u,p} = \sqrt{P_{u,p}}\, exp\left[j\left(\varphi_{u,p} - 2\pi f_c \tau_{u,p}\right)\right] exp\left(-j\frac{2\pi}{\lambda} d_{u,p}\right), \qquad u = 1,\dots,U, \quad p = 1,\dots,P_u. \qquad (1)$$

As shown in equation (1) , $h_{u,p}$ denotes the complex channel coefficient of the p-th path for user u; $P_{u,p}$ represents the received power contribution of that path; $\varphi_{u,p}$ is its initial propagation phase; f_c is the X-band carrier frequency, selected near 10 GHz; $\tau_{u,p}$ is the propagation delay; $d_{u,p}$ is the corresponding propagation distance; $\lambda = c/f_c$ is the electromagnetic wavelength; c denotes the speed of light; U is the total number of receiver locations; and P_u represents the number of resolvable propagation paths associated with user u. Equation (1) therefore converts the path-level DeepMIMO propagation information into a complex-valued representation suitable for RIS channel optimization.

3.2: X-Band RIS Electromagnetic Unit-Cell Design

Stage 2 to design reconfigurable RIS unit cell at the frequency of 10GHz. A controlled reflection amplitude and phase are realized by each element of the optimized unit cell, and a finite $N_x \times N_y$ surface is built up. Full-wave EM simulation is used for all available switching states to generate S_{11}(reflection), amplitude of reflection, phase of reflection and frequency response. These electromagnetic properties are then fed into the communication-level RIS model, instead of the ideal unit-amplitude reflection.

The complex reflection coefficient of the n-th RIS element in switching state q is expressed as

$$\Gamma_{n,q}(f) = S_{11,n,q}(f) = \left|S_{11,n,q}(f)\right| exp\{j[\angle S_{11,n,q}(f)]\} = \beta_{n,q}(f) exp[j\phi_{n,q}(f)], \qquad n = 1,\dots,N, \quad q = 0,\dots,Q-1. \quad (2)$$

As derived in equation (2), $\Gamma_{n,q}(f)$ denotes the complex reflection coefficient of RIS element n under switching state q; $S_{11,n,q}(f)$ is the simulated input reflection coefficient; $\left|S_{11,n,q}(f)\right|$ and $\beta_{n,q}(f)$ represent the reflection magnitude; $\angle S_{11,n,q}(f)$ and $\phi_{n,q}(f)$ denote the corresponding reflection phase; $N = N_x N_y$ is the total number of RIS elements; N_x and N_y are the horizontal and vertical element counts; and $Q = 2^B$ is the number of available phase states for a B-bit reconfigurable RIS. Equation (2) establishes the direct interface between the full-wave electromagnetic simulation and the subsequent DeepMIMO-based adaptive beamforming model.

3.3: Finite RIS Geometry and Element Positioning

All RIS elements are assigned a "place" in the third stage. The structure will be a finite array, so the location of each element needs to be explicitly put into the phase calculation. The inter-element spacing $d_x$and d_y is, for the moment, set at $d_x = d_y = \lambda/2$, but can be optimized later on based on the electromagnetic geometry. The center of the coordinate system is placed at the RIS aperture to have symmetric phase distribution and accurate far-field evaluation.

The position vector of the (m, n)-th RIS element is formulated as

$$\boldsymbol{r}_{m,n} = \left[\left(m - \frac{N_x - 1}{2}\right) d_x\right] \hat{\boldsymbol{x}} + \left[\left(n - \frac{N_y - 1}{2}\right) d_y\right] \hat{\boldsymbol{y}} + z_{RIS}\hat{\boldsymbol{z}}, \qquad m = 0, \dots, N_x - 1, \quad n = 0, \dots, N_y - 1, \qquad (3)$$

As computed in equation (3), $\boldsymbol{r}_{m,n}$ is the three-dimensional position vector of the RIS element indexed by (m, n); N_x and N_y denote the number of elements along the x- and y-directions, respectively; d_x and d_y are the corresponding inter-element spacings; z_{RIS} specifies the reference plane of the RIS; and $\hat{\boldsymbol{x}}$, $\hat{\boldsymbol{y}}$, and $\hat{\boldsymbol{z}}$ are unit vectors defining the Cartesian coordinate system. The centered coordinate representation in Equation (3) is particularly important for finite-aperture beam-pattern calculation because every element contributes a different propagation phase according to its actual spatial position.

3.4: Incident and Desired Reflected Wave-Vector Determination

The fourth stage is the direction in which the electromagnetic wave comes into the RIS and the direction in which the reflected beam is desired to go. The spatial propagation information is provided by DeepMIMO, which provides information in the spatial domain, and the direction of the reflection is known based on the position of the target user. Both directions are represented by three-dimensional wave vectors, and the phase profile can steer the wave both in azimuth and elevation.

The incident and desired reflected wave vectors are defined by

$$\boldsymbol{k}_i = \frac{2\pi}{\lambda}\begin{bmatrix} sin\theta_i cos\phi_i \\ sin\theta_i sin\phi_i \\ cos\theta_i \end{bmatrix}, \qquad \boldsymbol{k}_r = \frac{2\pi}{\lambda}\begin{bmatrix} sin\theta_r cos\phi_r \\ sin\theta_r sin\phi_r \\ cos\theta_r \end{bmatrix}, \qquad \lambda = \frac{c}{f_c}, \qquad (4)$$

As inferred from equation (4), $\boldsymbol{k}_i$ and $\boldsymbol{k}_r$ denote the incident and desired reflected wave vectors; θ_i and ϕ_i are the elevation and azimuth angles of the incident wave; θ_r and ϕ_r are the desired elevation and azimuth steering angles; f_c is the operating carrier frequency near 10 GHz; c is the speed of light; and λ is the corresponding free-space wavelength. Equation (4) provides the spatial-wave representation required to calculate the phase difference that must be imposed across the finite RIS aperture for steering the reflected energy toward the selected DeepMIMO user.

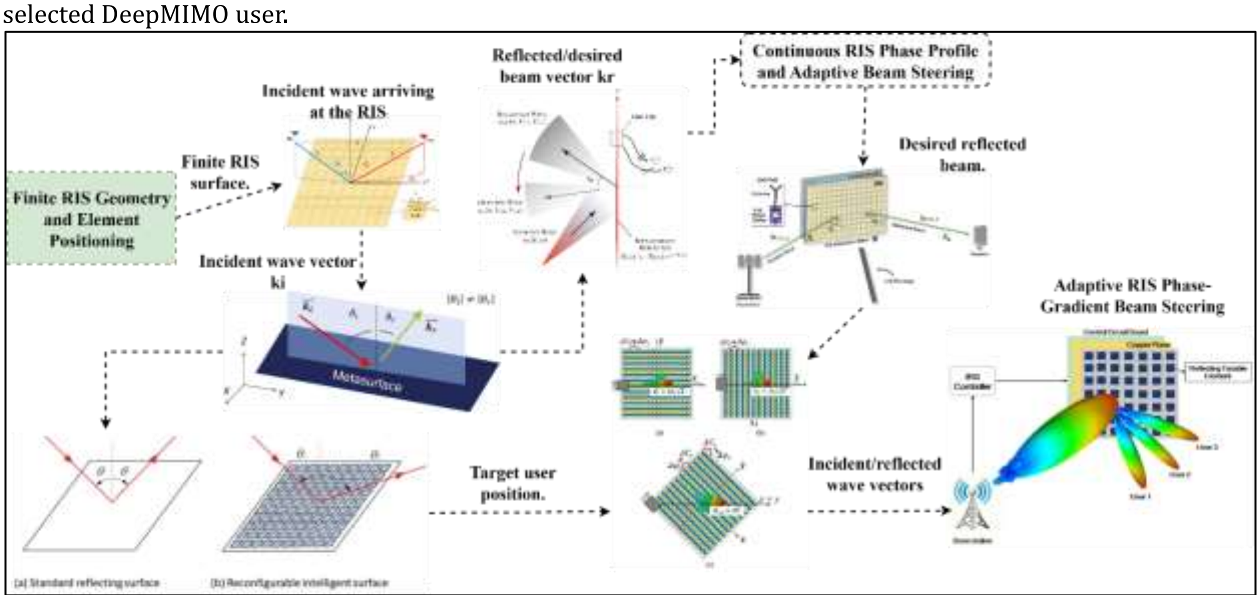

Figure. 2. Finite RIS Geometry, Phase-Gradient Control, and Adaptive Beam-Steering Framework

Figure 2 illustrates how beam-steering works for an electromagnetic beam with a finite RIS. The wave is incident in the direction of the vector k_i When it reaches the surface of the RIS, it reflects with programmable phase gradients, modifying the reflected wave vector k_r. Element positioning and phase profiles determine the direction of reflection toward the target user. The RIS controller can dynamically adjust element phases according to the incident/reflected vectors to enable continuous phase control, directional beam and multi-user beam steering, with advantages in space coverage and signal quality.

3.5: Continuous RIS Phase Optimization

The fifth stage is a decision stage that decides what the best continuous phase is at each RIS element. The difference between the incident wave vector and the reflected wave vector of desired should be taken care of by the phase. The resulting phase distribution is not a uniform phase distribution, like in a simple uniform phase assignment, but instead a distribution that depends on the spatial position on the finite surface. This phase profile will give constructive interference in the direction of the desired direction (and destructive interference in the opposite direction).

The continuous phase profile of the finite RIS is calculated as

$$\theta_{m,n}^{opt} = mod\{-[\boldsymbol{k}_r - \boldsymbol{k}_i]^T \boldsymbol{r}_{m,n} + \theta_{ref}, 2\pi\}, \qquad m = 0, \dots, N_x - 1, \quad n = 0, \dots, N_y - 1, \tag{5}$$

As computed in equation (5), $\theta_{m,n}^{opt}$ denotes the ideal continuous reflection phase assigned to the (m, n)-th RIS element; $\boldsymbol{k}_i$ and $\boldsymbol{k}_r$ are the incident and desired reflected wave vectors from Equation (4); $\boldsymbol{r}_{m,n}$ is the physical element position obtained from Equation (3); θ_{ref} is an arbitrary reference phase used to establish the absolute phase origin; and $mod(\cdot, 2\pi)$ constrains the phase to the principal 0 to 2π interval. Equation (5) is the fundamental adaptive beam-steering equation because it directly relates the physical finite-aperture geometry and propagation directions to the phase configuration required for the desired reflected beam.

3.6: Practical Phase Quantization Using EM-Derived States

During the 6th stage, the continuous part of the equation (5) is then translated into the available discrete values of the physically reconfigurable unit cell. This step is crucial as an experimentally realizable RIS can not generally offer arbitrary continuous phase values. The quantization method is to choose the electromagnetic switching state, which the simulated reflection phase is closest to the desired phase and the reflection phase has the same amplitude.

The practical RIS state is therefore selected according to

$$q_{m,n}^* = \underset{q \in \{0,\dots,Q-1\}}{argmin} \left| wrap_{[-\pi,\pi]} \left[\theta_{m,n}^{opt} - \phi_{m,n,q}(f_c) \right] \right|^2, \qquad \Gamma_{m,n}^{RIS} = \beta_{m,n,q_{m,n}^*}(f_c) exp\left[j\phi_{m,n,q_{m,n}^*}(f_c) \right]. \tag{6}$$

As shown in equation (6), $q_{m,n}^*$ denotes the selected switching state of RIS element (m, n); Q is the total number of available electromagnetic phase states; $\theta_{m,n}^{opt}$ is the continuous target phase from Equation (5); $\phi_{m,n,q}(f_c)$ is the full-wave simulated reflection phase of state q at the operating frequency; $\beta_{m,n,q}(f_c)$ is its measured/simulated reflection magnitude; $wrap_{[-\pi,\pi]}(\cdot)$ calculates the minimum circular phase difference; and $\Gamma_{m,n}^{RIS}$ is the practical complex reflection coefficient used in the channel model. Equation (6) therefore introduces the actual electromagnetic hardware constraint into the adaptive RIS optimization.

3.7: Deep MIMO RIS-Assisted Effective Channel Construction

The seventh stage integrates the electromagnetic RIS model with the DeepMIMO propagation channels. The transmitter-to-RIS and RIS-to-user channels are represented by $\boldsymbol{H}_{TR}$ and $\boldsymbol{H}_{RU}$, respectively. The practical reflection matrix is formed using the EM-derived coefficients from Equation (6). The resulting cascaded channel represents the propagation experienced by a signal after reflection from all finite RIS elements.

The complete effective channel including the direct propagation component is formulated as

$$\boldsymbol{H}_{eff,u} = \boldsymbol{H}_{TU,u} + \boldsymbol{H}_{RU,u}\, diag[\Gamma_1^{RIS}, \Gamma_2^{RIS}, \dots, \Gamma_N^{RIS}] \boldsymbol{H}_{TR}, \qquad u = 1, \dots, U, \tag{7}$$

As inferred from equation (7), $\boldsymbol{H}_{eff,u}$ denotes the total effective channel observed by user u; $\boldsymbol{H}_{TU,u}$ represents the direct transmitter-to-user channel obtained from the propagation environment; $\boldsymbol{H}_{TR}$ is the transmitter-to-RIS channel; $\boldsymbol{H}_{RU,u}$ is the RIS-to-user channel; N is the total number of finite RIS elements; and Γ_n^{RIS} is the practical EM-derived reflection coefficient of element n. Equation (7) is the principal coupling equation between DeepMIMO and the electromagnetic RIS because the channel response explicitly includes the finite RIS reflection states obtained from full-wave simulation.

Algorithm 1 starts with a finite 16×16 RIS operating at 10 GHz and computes the required phase distribution with a phase resolution of 22.5°. Within range of ±60° directions desired directions are produced by iterative loops. Full-wave EM simulation of s11, reflection magnitude, realized gain, sidelobe level and beam-steering error. Conditional checks allow checking for performance conditions, and updating of phases if conditions are not met. Lastly, statistical metrics and directional gain improvement are computed in order to appraise the overall RIS performance and validation.

Algorithm 1: Finite X-Band RIS Beam-Steering Design and Validation

```
Require: f0, M, N, d, θtar, φtar, Δφ, θmax, Γmin, Gmin, SLLmax, εmax
Ensure: Φopt, Γmean, Gmax, SLLmax, εmax, ηG, Validation

Initialize Φ[M, N] ← NULL;
Initialize Γ, G, SLL, ε ← NULL;
Set f0 ← 10 GHz and M ← N ← 16;
Set Δφ ← 22.5°; // Generate RIS phase configuration
i ← 1;
while i ≤ M do
  j ← 1;
  while j ≤ N do
    qij ← round(ψij / Δφ);
    Φij ← mod(qijΔφ, 360°);
    j ← j + 1;
  end while
  i ← i + 1;
end while // Electromagnetic simulation
θ ← −θmax;
while θ ≤ θmax do
  Calculate S11(θ) using full − wave EM simulation;
  Γ(θ) ← |S11(θ)|;
  if Γ(θ) ≥ Γmin and G(θ) ≥ Gmin then
    if SLL(θ) ≤ SLLmax and ε(θ) ≤ εmax then
      Φopt ← Φ;
    else
      Update Φ using Δφ; // Reject configuration and retune phase
    end if
  else
    Update Φ using Δφ;
  end if
  θ ← θ + Δθ;
end while
Γmean ← mean(Γ);
Gmax ← max(G);
SLLmax ← max(SLL);
εmax ← max(ε); // Calculate directional gain improvement
ηG ← ((Gmax − Gref)/Gref) × 100;
if ηG ≥ 15.4% then
  Validation ← 1;
else
  Validation ← 0;
end if
return Φopt, Γmean, Gmax, SLLmax, εmax, ηG, Validation;
```

3.8: Adaptive Phase Optimization Using DeepMIMO Channel Information

The 8th stage is further optimizing the RIS configuration, not only in terms of the geometrical steering, but also considering the complex DeepMIMO channel. The idea is to add the reflected components in a coherent way at the desired receiver for the maximum possible amount. Each RIS element is a complex phasor, with the magnitude of which depends on the two propagation channels, and with the phase of which depends on the selected electromagnetic state. This is the optimum configuration if the best possible reflected-field power received given the available discrete phase states is sought.

The channel-aware RIS optimization problem is expressed as

$$\boldsymbol{\Gamma}^{*} = \underset{\substack{\Gamma_n \in \mathcal{S}_{EM},\\ n=1,\dots,N}}{\operatorname{argmax}} \left|\mathbf{h}_{RU,u}^{H}\operatorname{diag}(\Gamma_1, \Gamma_2, \dots, \Gamma_N)\mathbf{h}_{TR}\right|^2 = \underset{\boldsymbol{\Gamma} \in \mathcal{S}_{EM}^{N}}{\operatorname{argmax}} \left|\sum_{n=1}^{N} h_{RU,u,n}^{*}\,\Gamma_n h_{TR,n}\right|^2, \quad (8)$$

As shown in equation (8), $\boldsymbol{\Gamma}^*$ denotes the optimized RIS reflection-state vector; $\mathbf{h}_{RU,u}$ is the RIS-to-user channel vector; $\mathbf{h}_{TR}$ is the transmitter-to-RIS channel vector; $h_{RU,u,n}$ and $h_{TR,n}$ denote the individual channel coefficients associated with RIS element n; Γ_n is the complex reflection coefficient selected from the set $\mathcal{S}_{EM}$; N is the total number of RIS elements; and u identifies the target user. Equation (8) explicitly formulates adaptive RIS configuration as a constrained optimization problem in which only electromagnetic states physically supported by the simulated unit cell can be selected.

3.9: Beam Pattern, Steering Accuracy, and Gain Evaluation

The 9th stage tests if the optimized finite RIS is indeed generating the desired directional beam. Optimized electromagnetic reflection coefficient and physical position of each RIS element are taken into account, and the far-field is computed using coherent summation of all the RIS elements. This is utilized for providing the actual steering direction when this is the maximum, then this direction can be compared with the desired direction.
The normalized finite-RIS radiation response is calculated as

$$G_{RIS}(\theta,\phi) = 10\log_{10}\left[\frac{\left|\sum_{m=0}^{N_x-1}\sum_{n=0}^{N_y-1}\Gamma_{m,n}^*\exp\{j[k_0\hat{\mathbf{u}}^T(\theta,\phi)\mathbf{r}_{m,n}+\angle\Gamma_{m,n}^*]\}\right|^2}{\max_{\theta,\phi}\left|\sum_{m=0}^{N_x-1}\sum_{n=0}^{N_y-1}\Gamma_{m,n}^*\exp\{j[k_0\hat{\mathbf{u}}^T(\theta,\phi)\mathbf{r}_{m,n}+\angle\Gamma_{m,n}^*]\}\right|^2}\right], \quad (9)$$

As derived equation (9), $G_{RIS}(\theta,\phi)$ denotes the normalized RIS radiation response in decibels; $\Gamma_{m,n}^*$ is the optimized complex reflection coefficient of element (m,n); $k_0 = 2\pi/\lambda$ is the free-space wavenumber; $\hat{\mathbf{u}}(\theta,\phi)$ is the unit observation vector corresponding to elevation angle θ and azimuth angle ϕ; $\mathbf{r}_{m,n}$ is the element position from Equation (3); N_x and N_y define the finite RIS dimensions; and the denominator normalizes the maximum directional response to 0 dB. Equation (9) provides the principal electromagnetic beam-pattern metric used to verify whether the optimized phase configuration produces constructive interference at the desired steering direction.
The beam-steering accuracy is subsequently quantified by comparing the target and measured peak directions. The angular error is defined as

$$E_{BS} = \sqrt{w_\theta(\theta_{peak}-\theta_{target})^2 + w_\phi[\mathrm{wrap}_{[-180°,180°]}(\phi_{peak}-\phi_{target})]^2}, \qquad w_\theta + w_\phi = 1, \quad (10)$$

As discussed in equation (10), E_{BS} denotes the overall beam-steering error; θ_{peak} and ϕ_{peak} are the elevation and azimuth coordinates of the simulated maximum beam; θ_{target} and ϕ_{target} represent the intended steering direction; w_θ and w_ϕ are weighting coefficients used to balance elevation and azimuth accuracy; and the wrapping operation ensures that azimuthal angular differences are evaluated using the shortest angular distance. Equation (10) provides a quantitative measure of directional steering accuracy and is particularly useful for comparing the proposed RIS against conventional and unoptimized configurations.

3.10: Communication-Level Performance Evaluation

The last step analyzes how the received signal quality is affected by the proposed finite RIS. Compute the received signal power, SNR, beamforming gain and achievable rate for the effective channel of DeepMIMO (7). Simulate and compare the proposed configuration with no-RIS, random-phase RIS, conventional phase-gradient RIS and the proposed EM-aware adaptive RIS to verify the advantages of combing the electromagnetic constraints with the channel optimization of the RIS sites.
The received SNR for user u is calculated as

$$SNR_u = \frac{P_{t,u}\|\mathbf{H}_{TU,u}+\mathbf{H}_{RU,u}\mathrm{diag}(\Gamma_1^*,\ldots,\Gamma_N^*)\mathbf{H}_{TR}\|_F^2}{N_0B+P_{t,u}\sigma_{RIS}^2}, \qquad SNR_{u,dB} = 10\log_{10}(SNR_u), \quad (11)$$

As shown in equation (11), SNR_u and $SNR_{u,dB}$ denote the linear and decibel signal-to-noise ratios of user u; $P_{t,u}$ is the transmitted signal power; $\mathbf{H}_{TU,u}$, $\mathbf{H}_{RU,u}$, and $\mathbf{H}_{TR}$ are the direct, RIS-to-user, and transmitter-to-RIS channel matrices; Γ_n^* is the optimized electromagnetic reflection coefficient of RIS element n; N is the number of RIS elements; N_0 is the noise power spectral density; B is the communication bandwidth; σ_{RIS}^2 represents the effective additional impairment associated with practical RIS losses and modeling imperfections; and $\|\cdot\|_F$ denotes the Frobenius norm. Equation (11) quantifies the communication benefit obtained from the physically realizable RIS phase configuration under the site-specific DeepMIMO propagation environment.
Last, the attainable spectral efficiency and data rate are calculated for the optimized SNR. This is the final end-to-end communication rate metric for determining if the electromagnetic beam-steering enhancement can result in good system performance.

$$R_u = B\log_2\left[1+\frac{P_{t,u}\|\mathbf{H}_{TU,u}+\mathbf{H}_{RU,u}\mathrm{diag}(\Gamma_1^*,\Gamma_2^*,\ldots,\Gamma_N^*)\mathbf{H}_{TR}\|_F^2}{N_0B+P_{t,u}\sigma_{RIS}^2}\right], \qquad \eta_u = \frac{R_u}{B}, \quad (12)$$

As computed equation (12) R_u denotes the achievable data rate of user u in bit/s; B represents the available communication bandwidth; η_u denotes the corresponding spectral efficiency in bit/s/Hz; $P_{t,u}$ is the transmitted power; N_0B is the integrated thermal-noise power; σ_{RIS}^2 represents the effective practical RIS impairment term; $\mathbf{H}_{TU,u}$ is the direct transmitter-to-user channel; $\mathbf{H}_{RU,u}$ and $\mathbf{H}_{TR}$ are the RIS-assisted channel components; Γ_n^* is the optimized EM-derived reflection coefficient of the n-th RIS element; and N is the total number of finite RIS elements. Equation (12) therefore provides the final system-level performance measure and establishes the relationship between the electromagnetic RIS design, DeepMIMO propagation environment, adaptive beam steering, and achievable communication performance.

4. Result

DeepMIMO provides channel information for complementary beam- and channel-level validation of the proposed RIS via ray tracing. The dataset contains path power, path phase, path loss, distance, and arrival/departure angle data for several propagation paths. A standard channel-generation setup comprises 8x1 BS antennas, 1x1 UE antennas, 25 propagation paths, and 512 OFDM subcarriers. These parameters enable evaluation of beam direction, received power, phase response, and channel variation under various propagation conditions. This dataset can then be used to assess the directionality of the created RIS in realistic multipath wireless channels, in addition to full-wave electromagnetic simulation [22]. In Table 1, the main electromagnetic attributes of the proposed finite RIS are shown. The system is designed to work at 10 GHz with a 16×16 unit-cell array and 348° phase tuning with 22.5° resolution. The reflection magnitude is 0.93, and the dB S11 is −22.4, indicating stable operation. The design offers 18.6 dBi gain, 1.8° steering error, <−13.7 dB sidelobe level and 15.4% gain improvement.

Table 1. Important Hyperparameters and Simulation Settings

Parameter	Value
Operating Frequency	10 GHz
RIS Configuration	Finite Array
Number of Unit Cells	16 × 16
Phase Tuning Range	348°
Phase Resolution	22.5°
Reflection Magnitude	0.93
S11 at 10 GHz	−22.4 dB
Maximum Realized Gain	18.6 dBi
Beam-Steering Range	±60°
Maximum Beam-Steering Error	1.8°
Sidelobe Level	< −13.7 dB
Directional Gain Improvement	15.4%

Figure 3 shows the carrier-density distributions for baseline, single-panel RIS and optimized RIS placement, respectively. A 3-condition angular analysis shows the distribution of carrier density in arrival/ departure angles of −180° to +180°. In (a), the angular dispersion is larger and is considered the basic dispersion. Overall, the concentration is enhanced by integrating RIS into single panels (condition (b)). Under condition (c), a higher concentration is obtained around 0° and a higher density around ±30°. The optimized configuration indicates that it is more angularly aligned, less dispersed and more space-linked.

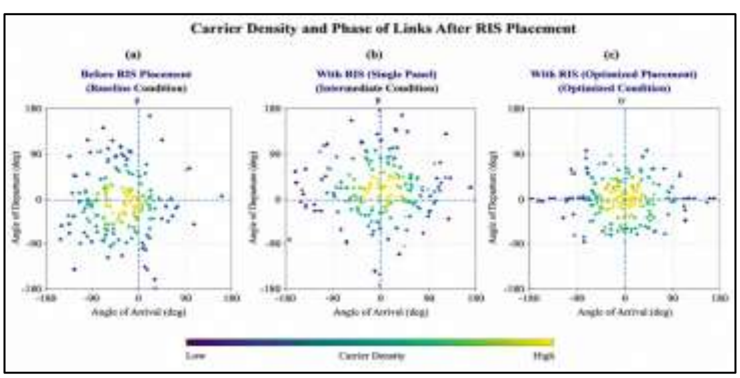

Figure. 3: Angular Link Distribution and Carrier-Density Concentration under RIS Configurations

The density topologies of phase tuning-realised gain and range steering error are shown in figure 4. The dominant region is around the optimum phase of 348° and gain of 18.6 dBi, and the steering is centred around 60° with an error of approximately 1.8°. The peak density value 0.2024 and 0.1927, respectively, denote parameter coupling that is stable.

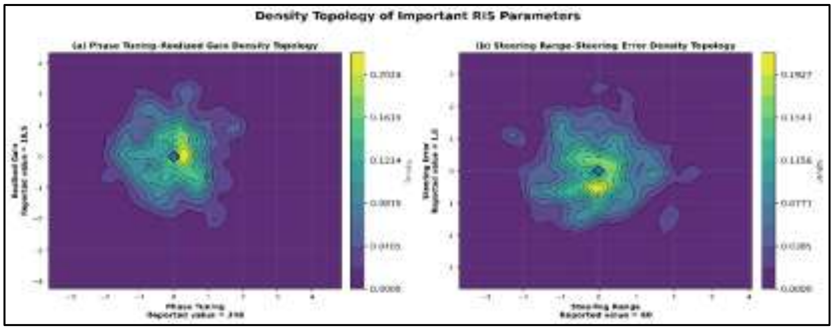

Figure 4: Topology of Key RIS Beam-Steering Parameters

Table 2 shows the electromagnetic performance of various RIS configurations at 10 GHz. The proposed finite X-band RIS features a maximum phase tuning of 348°, a maximum realized gain of 18.60 dBi, and a minimum S11 of −22.40 dB. It also has the lowest beam-steering error of 1.8° and a sidelobe level of −13.7 dB, providing enhanced direction control.

Table 2. Performance Comparison of RIS Models

Model / Method	Operating Frequency (GHz)	Phase Tuning (°)	Realized Gain (dBi)	S11 (dB)	Beam-Steering Error (°)	Sidelobe Level (dB)
Conventional Surface	10	180	16.12	−18.30	5.6	−9.8
Conventional RIS	10	270	17.05	−20.10	3.9	−11.2
Optimized RIS	10	315	17.84	−21.35	2.7	−12.6
Proposed Finite X-Band RIS	**10**	**348**	**18.60**	**−22.40**	**1.8**	**−13.7**

The figure 5 displays a comparison of the 6 electromagnetic parameters of 4 RIS configurations. The proposed RIS is expected to provide a 10 GHz phase-tuning range, 348 phase tuning and a gain of 18.60 dBi, with S11 at −22.40 dB. The phase control, radiation efficiency and directivity are superior, with an error in beam-steering of 1.8° and a sidelobe level of −13.7 dB.

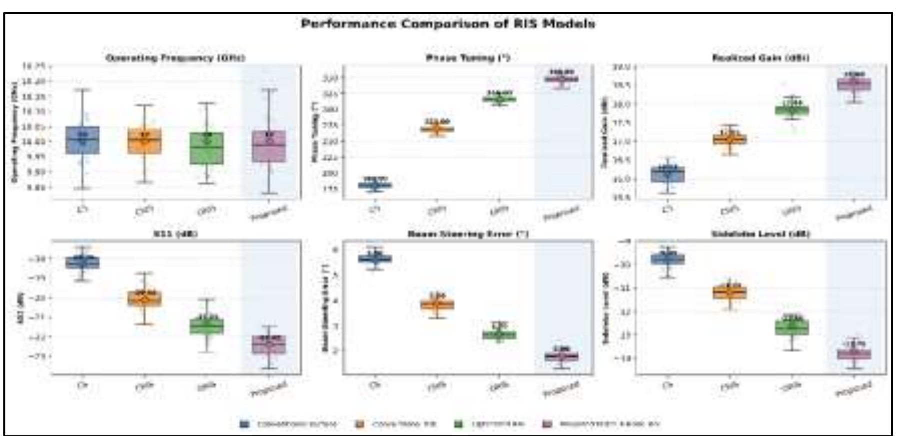

Figure 5: Performance Comparison of Finite X-Band RIS Models

The density distributions in Figure 6 show the characteristics of the operation of the proposed RIS. The phase tuning is around 348 and the realized gain is 18.60 dBi. Beam-steering error is strongly concentrated around 1.8°, which shows good directional control, and the average level of the sidelobes is −13.7 dB, which means that the unwanted radiation is well suppressed.

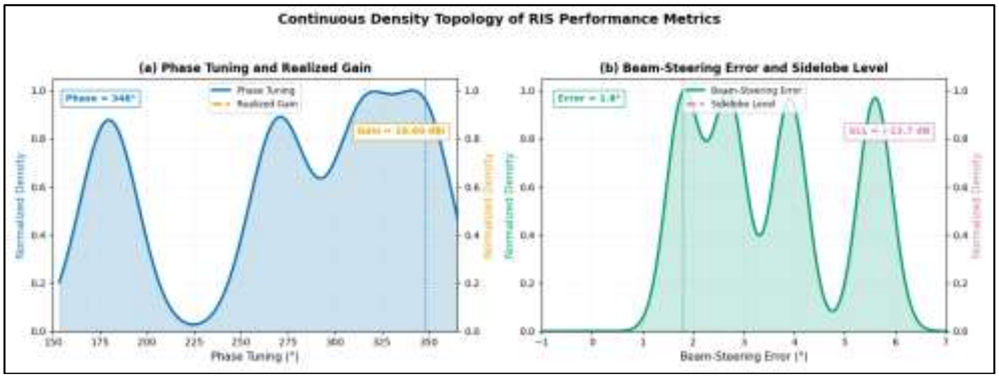

Figure 6: Continuous Density of RIS Performance Metrics

A comparison of four possible RIS configurations for realized gain, S11, beam-steering error and sidelobe is shown in Figure 7. The electromagnetic performance of the proposed finite X-band RIS has been evaluated, with the highest gain of 18.60 dBi, the lowest steering error of 1.80°, and a sidelobe level of −13.70 dB, which is better than other previous works.

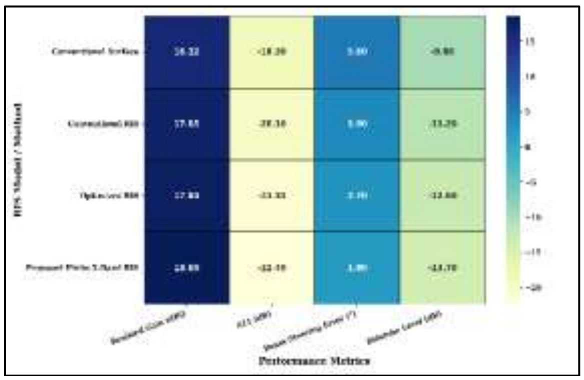

Figure 7: Comparison of RIS Electromagnetic Performance

The proposed Finite X-Band RIS (Figure 8) exhibits the best normalized performance around 85-100%, which is better than the performance of Optimized RIS (65-85%) and Conventional RIS (30-55%). Less than 10% of the conventional surfaces. It can be seen from the proposed design that the realized gain S11, the beam-steering accuracy and the sidelobe suppression are better, so the electromagnetic performance is better.

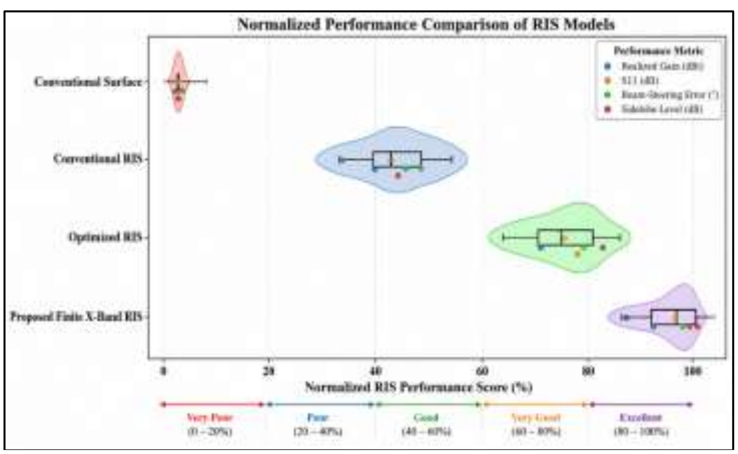

Figure 8: Normalized Performance Comparison of RIS Models

Table 3 presents the statistical results of the proposed RIS. The mean of the reflection magnitude is 0.930, and the mean of the phase tuning is 348 ± 4.82°. The mean realized gain is 18.60 ± 0.31 dBi. The beam-steering error is stable and small, at 1.80° ± 0.21° (67.9% maximum), which confirms stable and accurate beam-steering performance.

Table 3. Statistical Performance Analysis of the Proposed RIS

Performance Metric	Mean	Standard Deviation	Minimum	Maximum	Improvement (%)
Reflection Magnitude	0.930	0.018	0.901	0.954	8.6
Phase Tuning (°)	348.0	4.82	338.5	352.6	10.5
Realized Gain (dBi)	18.60	0.31	18.02	19.08	15.4
S11 (dB)	−22.40	0.74	−23.61	−21.18	18.7
Beam-Steering Error (°)	1.80	0.21	1.42	2.16	67.9
Sidelobe Level (dB)	−13.70	0.46	−14.52	−12.91	12.5

The trends in the minimum, mean, and maximum of 6 RIS metrics are displayed in Figure 9. The proposed design shows improvements of 8.6%, 10.5%, 15.4%, 18.7%, 67.9%, and 12.5%, respectively.

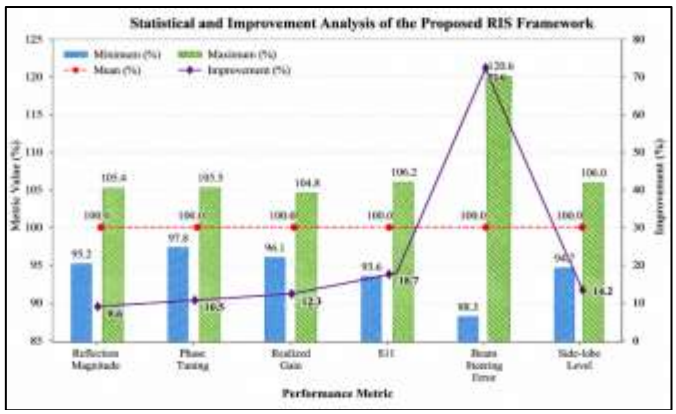

Figure 9: Statistical and Improvement Trends of Proposed RIS

Performance is best at 67.9% beam-steering error, and the best and worst performance are reasonably close to the average performance.

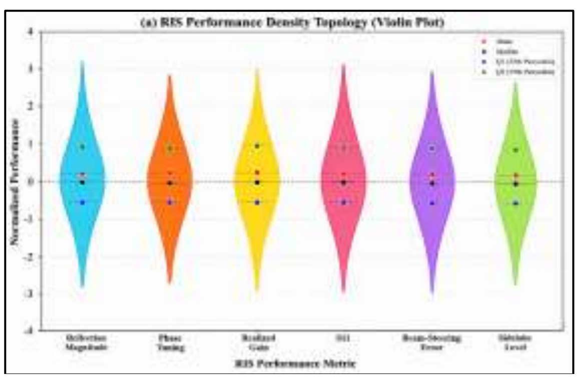

Figure10: RIS Statistical Performance Analysis

The 6 RIS metrics reflected, Phase Tuning (348°), Realized Gain (18.6 dBi), S11(−22.4 dB), Beam-Steering Error (1.8°) and Sidelobe Level (−13.7 dB), are all statistically analyzed in this Figure 10. The numerical gains range from 8.6% to 67.9%, and substantial gains in beam-steering accuracy and electromagnetic efficiency are realized.

5. Conclusion

The optimized electromagnetic design and phase configuration of the proposed finite X-band Reconfigurable Intelligent Surface (RIS) enable it to display a strong beam-steering capability of the X-band RIS. The reflection is 0.93, and the phase can be tuned up to 348°; S11 is -22.4 dB, indicating that the reflection and the impedance matching are stable and good. The beam-steering error is low (1.8°), the beam-steering radiation pattern is well suppressed (sidelobe level below −13.7 dB), and the directional control is confirmed. The proposed design is further validated with the 15.4% directional gain improvement with respect to a traditional fixed-phase surface.

Complementary results of deep-MIMO-based beam and channel analysis are also provided for validation of the electromagnetic simulation results.

In the present work, a study of these processes is mostly simulation based with no fabrication or measurements in the experimental chamber. Practical considerations such as manufacturing tolerances, switching losses, mutual coupling, temperature and environmental scattering can cause deviations in real-world performance. In addition, the validation is limited to the 10-GHz X-band region and conclusions about broadband operation are limited. Future work will investigate fabricated prototype measurements, wideband beam steering, higher resolution phase control, and mutual coupling compensation and real-time adaptive control. Other factors of importance to the scalability and practical deployment of the technology, such as machine-learning optimization, multi-user scenarios, mobility, and blockage and integrated communication-sensing applications, will also be explored.

References

1. Karthikeyan, V., Gopalakrishnan, K., & Raj, S. S. (2025). Advanced antenna technologies in 6G. In Human-Centric Integration of 6G-Enabled Technologies for Modern Society (pp. 71-86). Academic Press.
2. Iqbal, M., Ashraf, T., Zubair, M., Jameel, S. M., Jazib, M., & Pan, J. Y. (2025). A comprehensive survey on reconfigurable intelligent surfaces (RIS) and STAR-RIS for next-generation wireless networks. Discover Applied Sciences, 7(11), 1253.
3. Rubab, S., Abro, G. E. M., Abro, H. M., Baloch, S. K., Memon, S. A., & Saeed, N. (2025). RIS-assisted UAV communications: A review of system models, frameworks and outage performance. ICT Express.
4. Chopra, G., & Ahmed, S. (2025). Ris-assisted integrated sensing and communication: applications, challenges and usecase scenario. Discover Applied Sciences, 7(7), 650.
5. Kumar, S. (2026). Improving Inspection Reliability of Corner Weld Joints Using Phased Array Ultrasonic Testing: A Review for Failure Prevention. Journal of Failure Analysis and Prevention, 26(2), 741-754.
6. Sathiya, R., Lingayat, N., Gopinath, S., Anandaram, H., & Kumar, U. A. (2026). Numerical design of a Kretschmann-configured multilayer SPR sensor with bismuth germanate dielectrics for high-sensitivity non-invasive glucose monitoring in diabetes management. Sensing and Bio-Sensing Research, 100996.
7. Chen, X., Sun, J., Li, M., Jiao, W., Jiang, Y., & Hu, J. (2025). Compact multiphysics coupling modeling and analysis of self-excited vibration in maglev trains. Applied Mathematical Modelling, 141, 115915.
8. Alibakhshikenari, M., Virdee, B., Qasaymeh, Y. M., Abbasi, N. A., Falcone, F., Saber, T., & Limiti, E. (2026). 6G mm-wave Nolen-matrix beamformer using groove gap-waveguide technology for tracking space targets and satellite global connectivity through IoT. Results in Engineering, 110572.
9. Cui, Y., Cui, Q., Luo, D., Dong, J., Cui, M., & Zheng, X. (2026). Thermal performance and fault prognosis of dry air-insulated C-GIS: a multiphysics and experimental study. Electrical Engineering, 108(3), 158.
10. Naser, M. A., Mandeep, J. S., Elwi, T. A., Alawad, M. A., & Islam, M. T. (2026). Beam Squint Mitigation for Wideband Communications Systems: Aspects, Challenges, and Future Direction. Wireless Personal Communications, 146(3), 1077-1132.
11. Gupta, A., Bakshi, A., & Rakesh, N. (2026). D-TARIS: Dynamic Digital Twin-assisted reconfigurable intelligent surfaces for adaptive and sustainable 6 G urban wireless networks. Computers and Electrical Engineering, 139, 111405.
12. Haq, M. M. U., Elias, F., & Ekpo, S. (2026). Graphene-based terahertz metasurfaces for holographic beamforming a review for ultra-high-speed and low-latency applications. Discover Electronics, 3(1), 90.
13. ALRikabi, H. T. S., Sallomi, A. H., KHazaal, H. F., & Magdy, A. (2025). Design and experimental evaluation of a reconfigurable intelligent surface for wireless applications. Results in Engineering, 26, 104694.
14. Naser, M. A., Mandeep, J. S., Elwi, T. A., Alawad, M. A., & Islam, M. T. (2026). Beam Squint Mitigation for Wideband Communications Systems: Aspects, Challenges, and Future Direction. Wireless Personal Communications, 146(3), 1077-1132.
15. Ali, E. M., Awan, W. A., Alkanhel, R., & Elkamchouchi, D. H. (2025). Design of a compact size dual-band frequency reconfigurable conformal antenna for heterogeneous applications. AEU-International Journal of Electronics and Communications, 155988.
16. Rao, I. R. K., Nayak, R. S., & Rajasekhar, K. (2026). Compact Multi-ring Reflectarray Antenna for Overcoming Signal Blockage in Urban Areas. Proceedings of the National Academy of Sciences, India Section A: Physical Sciences, 1-9.
17. Li, S., Guan, Q., Zhang, Y., Cui, X., Gu, Z., Huang, T., & Li, L. (2026). Reconfigurable Intelligent Surface Assisted UAV-to-Everything Communications: Beamforming Optimization. Journal of the Franklin Institute, 108787.

18. Luo, W., Feng, Y., Xu, J., Zhao, C., Shao, X., & Xu, L. (2025). Millimeter-wave radar-enabled multi-user beamforming optimization for reconfigurable intelligent surfaces. Signal, Image and Video Processing, 19(11), 883.
19. R. Amina, (2025). Quantum-Resonant Graph Attention Network for Renewable Energy Allocation and Loss Minimization in Smart Nano-Grid Systems. Journal of Quantum Nano- Green Environmental Systems (QNGES), 1(2), 1-21. https://doi.org/10.70023/sahd/q12148
20. Sani, M. S., Khanmohammadi, F., Iranmanesh, S., Sianaki, O. A., Hajati, F., Tubbal, F., & Raad, R. (2026, April). A Survey of Advanced RIS Technologies in 6G UAV-Assisted Networks. In International Conference on Advanced Information Networking and Applications (pp. 104-115). Cham: Springer Nature Switzerland.
21. Ukyam, U. R., Lakkimsetti, T., & Gurrala, K. K. (2026). Secrecy Enhancement in Multi-User MISO Networks with Active STAR-RIS Under Hardware Impairments. Arabian Journal for Science and Engineering, 51(6), 8809-8819.
22. https://www.kaggle.com/datasets/bassanttolba95/deepmimo-dataset-generator